Available online at www.sciencedirect.com
ScienceDirect
International Journal of Solids and Structures 44 (2007) 5481–5498
INTERNATIONAL JOURNAL OF SOLIDS AND STRUCTURES
www.elsevier.com/locate/ijsolstr

# Rupture mechanisms in combined tension and shear—Micromechanics

Imad Barsoum, Jonas Faleskog *

*Department of Solid Mechanics, Royal Institute of Technology, SE-100 44 Stockholm, Sweden*

Received 31 October 2006; received in revised form 8 January 2007
Available online 17 January 2007

Communicated by S. Kyriades

**Abstract**

A micromechanics model based on the theoretical framework of plastic localization into a band introduced by Rice is developed. The model consists of a planar band with a square array of equally sized cells, with a spherical void located in the centre of each cell. The periodic arrangement of the cells allows the study of a single unit cell for which fully periodic boundary conditions are applied. The micromechanics model is applied to analyze failure by ductile rupture in experiments on double notched tube specimens subjected to combined tension and torsion carried out by the present authors. The stress state is characterized in terms of the stress triaxiality and the Lode parameter. Two rupture mechanisms can be identified, void coalescence by internal necking at high triaxiality and void coalescence by internal shearing at low triaxiality. For the internal necking mechanism, failure is assumed to occur when the deformation localizes into a planar band and is closely associated with extensive void growth until impingement of voids. For the internal shearing mechanism, a simple criterion based on the attainment of a critical value of shear deformation is utilized. The two failure criteria capture the transition between the two rupture mechanisms successfully and are in good agreement with the experimental result.


*Keywords:* Micromechanics; Mixed mode ductile fracture; Rupture mechanisms; Void coalescence

## 1. Introduction

Recent experimental studies show that ductility depends markedly on the the type of rupture mechanism that is active (Bao and Wierzbicki, 2004; Barsoum and Faleskog, 2007). This is especially noticeable in the low to intermediate stress triaxiality regime, where stress triaxiality is defined as the ratio between mean stress and the effective von Mises stress. In this regime, triaxiality is not sufficient in order to accurately predict ductile rupture. Also, a parameter quantifying the type of stress deviator state appears to be necessary (Wierzbicki et al., 2005; Barsoum and Faleskog, 2007). The stress deviator state, can for an isotropic material and the

* Corresponding author. Tel.: +46 8 790 8977; fax: +46 8 411 2418.
*E-mail address:* jonasf@hallf.kth.se (J. Faleskog).

0020-7683/$ - see front matter 
doi:10.1016/j.ijsolstr.2007.01.010

purpose discussed here, fully be described by the third stress deviator invariant or by the Lode parameter. The latter describes the position of the middle principal stress in relation to the maximum and minimum principal stresses.

In Barsoum and Faleskog (2007), experiments are carried out on a double notched tube specimen subjected to a combination of tension and torsion, as shown in Fig. 1(a). In the notched region, Fig. 1(b), the average normal stress and the average shear stress are statically determined and given by the tensile force and the torque, respectively. The presence of the notch increases triaxiality and adds hydrostatic stress to the simple tension–torsion stress state in the centre of the notch. By applying different ratios of torsion and tension, stress triaxiality can be controlled and varied in the tests. Barsoum and Faleskog (2007) investigated two different structural steels, an intermediate strength steel and a high strength steel. For both materials they observe that when the stress triaxiality is sufficiently high, the specimens fail by a ductile rupture mechanism characterized by voids that have grown to impingement and coalesce by internal necking, as seen by the fractograph in Fig. 2(a). By contrast, when the stress triaxiality is sufficiently low, failure occurs by plastic shear localization in ligaments between voids, see fractograph in Fig. 2(b). Thus, in both cases the fracture surfaces are covered by voids. In this companion paper the authors develop a micromechanics model based on a layer of pre-existing voids to examine the transition between the two rupture mechanisms observed in Fig. 2.

The localized type of deformation characterizing both rupture mechanisms discussed above fits well into the general theoretical framework of plastic localization introduced by Rice (1977), where he investigates the conditions for deformation to localize into a thin band. Here, we make use of the kinematical conditions for the deformation across the band to analyze the transition between the two rupture mechanisms seen in Fig. 2. The deformation gradient is homogeneous outside the band in the Rice model, whereas it varies in a continuous manner with position across the band. This facilitates localization into a symmetric mode, a shear mode or a combination of both modes. The important effect of porosity on plastic flow localization and material softening have been studied by Needleman and Rice (1978), Yamamoto (1978) and Saje et al. (1982), where the influence of pre-existing voids and void nucleation within a continuum description are examined. Similarly, Tvergaard (1981, 1982a), Koplik and Needleman (1988), Faleskog and Shih (1997) and Pijnenburg and Van der Giessen (2001) used cell models with discrete voids to explore the influence of porosity on void coalescence and localization of plastic flow. Ductile rupture in smooth and notched plane strain and axisymmetric specimen configurations driven by evolution of porosity have been studied by Needleman and Tvergaard (1984) and Tvergaard and Needleman (1984). However, one of the main issues in the present study, the transition between the two rupture mechanisms, is not thoroughly addressed in the studies cited above.

In the present work, a micromechanics model was developed with the purpose to investigate the conditions that governs the transition between the two rupture mechanisms observed in the experiments by Barsoum and Faleskog (2007) and are shown in Fig. 2(a) and (b). This model is presented in Section 2, the properties of the materials used in the experiments are summarized in Section 3 and the general model behavior illustrating the two rupture modes are delineated in Section 4. The micromechanics analysis of the tests is presented in Section 5.

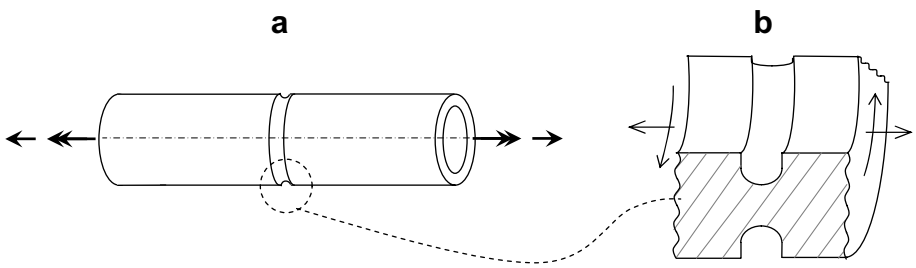


Fig. 1. (a) A schematic picture showing the double notched tube specimen loaded in combined tension and torsion used in Barsoum and Faleskog (2007). (b) A close-up of the notch region.

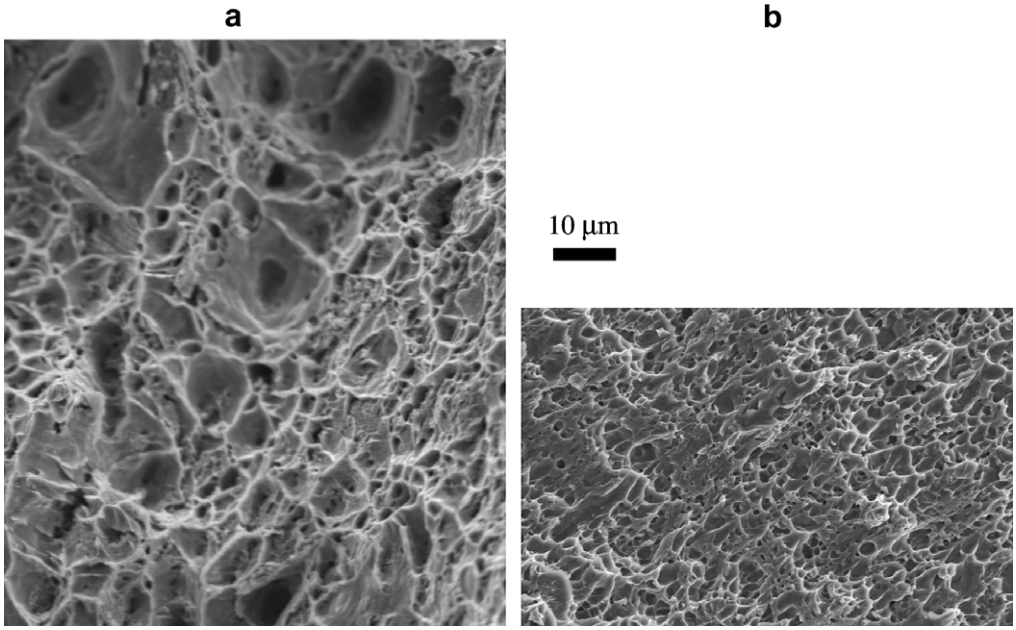


Fig. 2. Scanning electron microscope fractographs illustrating two different rupture mechanisms: (a) void coalescence by internal necking and (b) void coalescence by internal shearing. The fractographs are taken from fractured specimens of material Weldox 420 from tests conducted by Barsoum and Faleskog (2007).

## 2. Micromechanics model

To model failure in the tube experiment, we employ a micromechanics model where the material deforms under the macroscopic stress state of combined generalized tension and generalized shear as shown in Fig. 3(a). Material failure is assumed to occur when the deformation becomes highly non-uniform and localizes into a thin planar band. Furthermore, it is assumed that the mechanism leading to the onset of localized deformation and subsequent failure is ductile rupture involving nucleation, growth and coalescence of voids.

In the present study, the material is assumed to contain an initial planar band with a regular square array of pre-existing voids, see Fig. 3(a). Thus, the process of void nucleation is not considered. The pre-existing array of voids can be viewed as an initial imperfection, which may induce localization into a symmetric mode, a shear mode or a combination of both. The behavior of the matrix material is taken to be homogeneous,

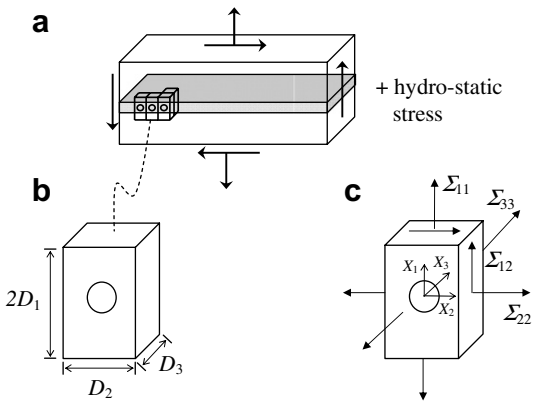


Fig. 3. Micromechanics model: (a) homogeneous material with a band containing pre-existing voids, (b) dimensions of the unit cell and (c) macroscopic stresses acting on the unit cell referring to a Cartesian coordinate system with origin at the centre of the void.

elastic–plastic with isotropic hardening and modeled by a finite strain $J_2$ flow theory. Building on the work by Marciniak and Kuczynski (1967), Rice (1977) presents a general framework for imperfection based localization analysis, as is also discussed in Needleman and Tvergaard (1992). The present micromechanical analysis fits well into the framework of Rice.

Due to the regular array of voids, attention can be restricted to a three-dimensional unit cell as indicated in Fig. 3(b) and (c), with linear dimensions $2D_1$, $D_2$ and $D_3$. The unit cell contains one void placed in its centre, initially of spherical shape with radius $R_0$. The initial size of the cell is given by $D_1 = D_2 = D_3 = D_0$. The initial ratio of void size to void spacing is defined as $\chi_0 = R_0/D_0$ and the initial void volume fraction in the cell can be expressed as $f_0 = \chi_0^3\pi/12$. In the present case, $\chi_0$ is the more relevant parameter for defining porosity.

### 2.1. 3D unit cell

The macroscopic Cauchy stresses $\Sigma_{ij}$ acting on the cell, see Fig. 3(c), are equal to the volume average of the Cauchy stresses, $\sigma_{ij}$, over the deformed volume $V$, and can be calculated as

$$\Sigma_{ij} = \frac{1}{V}\int_V \sigma_{ij}\,\mathrm{d}V. \tag{1}$$

The mean value and the von Mises effective value of the macroscopic stress are then defined as

$$\Sigma_\mathrm{h} = \frac{1}{3}(\Sigma_{11} + \Sigma_{22} + \Sigma_{33}), \tag{2}$$

$$\Sigma_\mathrm{e} = \frac{1}{\sqrt{2}}\sqrt{(\Sigma_{11} - \Sigma_{22})^2 + (\Sigma_{22} - \Sigma_{33})^2 + (\Sigma_{33} - \Sigma_{11})^2 + 6\Sigma_{12}^2}. \tag{3}$$

Loading is applied on the unit cell such that the macroscopic stresses acting on the cell follow the proportional history

$$\Sigma_{22}/\Sigma_{11} = \Sigma_{33}/\Sigma_{11} = \rho_\mathrm{n}, \quad \Sigma_{12}/\Sigma_{11} = \rho_\mathrm{s}, \tag{4}$$

where $\rho_\mathrm{n}$ and $\rho_\mathrm{s}$ are prescribed constants. By varying $\rho_\mathrm{n}$ and $\rho_\mathrm{s}$ a stress state of combined generalized tension and generalized shear can be accomplished. Furthermore, the stress triaxiality $T$ and the Lode parameter $\mu$ will remain constant during the load history as

$$T = \frac{\Sigma_\mathrm{h}}{\Sigma_\mathrm{e}} = \frac{(1 + 2\rho_\mathrm{n})\cdot \mathrm{sign}(\Sigma_{11})}{3\sqrt{(1-\rho_\mathrm{n})^2 + 3\rho_\mathrm{s}^2}}, \tag{5}$$

$$\mu = \frac{2\Sigma_\mathrm{II} - \Sigma_\mathrm{I} - \Sigma_\mathrm{III}}{\Sigma_\mathrm{I} - \Sigma_\mathrm{III}} = -\frac{(1-\rho_\mathrm{n})\cdot \mathrm{sign}(\Sigma_{11})}{\sqrt{(1-\rho_\mathrm{n})^2 + 4\rho_\mathrm{s}^2}}, \tag{6}$$

where $\Sigma_\mathrm{I} \geqslant \Sigma_\mathrm{II} \geqslant \Sigma_\mathrm{III}$ are the macroscopic Cauchy principal stresses. From Eqs. (5) and (6), the stress ratios can be expressed in terms of $T$ and $\mu$ as

$$\rho_\mathrm{n} = \frac{3T\sqrt{3+\mu^2} + 2\mu}{3T\sqrt{3+\mu^2} - 4\mu}, \quad \rho_\mathrm{s} = \frac{3\sqrt{1-\mu^2}}{3T\sqrt{3+\mu^2} - 4\mu}. \tag{7}$$

The solutions for $\rho_\mathrm{n}$ and $\rho_\mathrm{s}$ are valid for $-1 \leqslant \mu \leqslant 1$ and $\Sigma_{11} \gtrless 0$ for $T \gtrless 4\mu/(3\sqrt{3+\mu^2})$. A few limiting cases are here of interest. Those are: $\rho_\mathrm{n} = -1/2$ and $\rho_\mathrm{s} = -3\sqrt{1-\mu^2}/(4\mu)$ for $T \to 0$; $\rho_\mathrm{n} = 1$ and $\rho_\mathrm{s} = 1/(\sqrt{3}T)$ for $\mu \to 0$; $\rho_\mathrm{n} = (3T-1)/(3T+2)$ and $\rho_\mathrm{s} = 0$ for $\mu \to -1$.

Relative to a fixed Cartesian frame, a material point is described by the coordinates $X_i$ in the undeformed configuration and by the coordinates $x_i(X_k) = X_i + u_i(X_k)$ in the deformed configuration, where $u_i(X_k)$ denotes the displacements. Fig. 4(a) depicts how the 3D unit cell may deform under loading. It is a combination of two deformation modes—an axisymmetric mode and a shear mode, and as a consequence the cell boundaries will not remain straight. Thus, fully periodic boundary conditions must be applied on faces with normal vectors in the $X_2$–$X_3$ plane, which will be given in detail in Section 2.2. Sufficiently remote from the band of imperfection, i.e., the void, homogeneous conditions are assumed to prevail, where for instance $\partial u_1/\partial X_2 = \partial u_1/\partial X_3 = 0$.

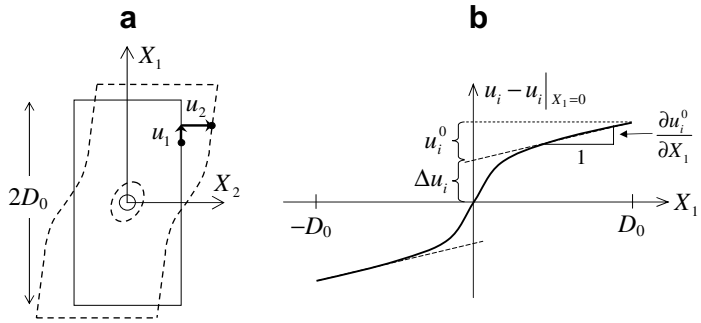


Fig. 4. (a) Depicting a general deformation mode of the unit cell in plane $X_3 = 0$ and (b) illustrating the uniform and non-uniform parts of the displacement, where $i = 1, 2$.

Such conditions are here assumed for the boundary surfaces $X_1 = \pm D_0$, which will remain straight throughout the loading.

Following the notation of Rice (1977), compatibility across the band requires in the present cell analysis that the displacement gradient along $X_1 = \pm D_0$ must take the form

$$\frac{\partial u_i}{\partial X_1} = \left(\frac{\partial u_i}{\partial X_1}\right)^{\circ} + q_i(X_1), \quad i = 1, 2, \tag{8}$$

where $()^{\circ}$ denotes the uniform field quantities outside the band of localized deformation and $q_i$ denotes the non-uniform part of the displacement gradient across the band, which is a function of $X_1$ only, see the illustration in Fig. 4(b). The volume average of the deformation gradient can be determined from the displacements on the cell boundary as

$$\bar{F}_{ik} = \frac{1}{V_0}\int_{V_0} F_{ik}\,\mathrm{d}V_0 = \delta_{ik} + \frac{1}{V_0}\int_{S_0} u_i n_k^0\,\mathrm{d}S_0, \tag{9}$$

where $V_0$ and $S_0$ are undeformed volume and outer surfaces of the cell, respectively, $\delta_{ik}$ denotes the Kronecker delta and $n_k^0$ is components of the normal vector to $S_0$ in the undeformed configuration. In view of Fig. 4(b) and Eqs. (8) and (9), the volume average of the deformation gradient for the 3D unit cell can be expressed as

$$\bar{\mathbf{F}} = \mathbf{F}^0 + \bar{\mathbf{F}}^q = \begin{bmatrix} F_{11}^0 + \bar{q}_1 & 0 & 0 \\ F_{21}^0 + \bar{q}_2 & F_{22}^0 & 0 \\ 0 & 0 & F_{33}^0 \end{bmatrix} \quad \text{with } \bar{q}_i = \frac{\Delta u_i}{D_0}. \tag{10}$$

Here, $\mathbf{F}^0$ denotes the uniform deformation gradient outside the band of localized deformation, and hence localization of deformation into a narrow planar band can be defined as (Needleman and Tvergaard, 1992)

$$\left\|\dot{\bar{\mathbf{F}}}\right\| \Big/ \left\|\dot{\mathbf{F}}^0\right\| \to \infty. \tag{11}$$

In Eq. (11) the norm $\|\|$ of a second order tensor with components $()_{ij}$ is evaluated as $\sqrt{()_{ij}()_{ij}}$, and for practical purposes localization is taken to occur when the ratio $\|\dot{\bar{\mathbf{F}}}\|/\|\dot{\mathbf{F}}^0\|$ is sufficiently large. In the present study, a ratio of 2 is used.

As an effective scalar measure of strain we will use

$$E_{\mathrm{e}} = \int \sqrt{\frac{2}{3}D'_{ij}D'_{ij}}\,\mathrm{d}t, \quad D'_{ij} = D_{ij} - \frac{1}{3}\delta_{ij}D_{kk}, \tag{12}$$

where $D_{ij}$ is the components of the volume average of the rate of deformation tensor, which can be calculated from the volume average of the deformation gradient as

$$D_{ij} = \frac{1}{2}(\dot{\bar{F}}_{ik}\bar{F}_{kj}^{-1} + \dot{\bar{F}}_{jk}\bar{F}_{ki}^{-1}). \tag{13}$$

### 2.2. Numerical implementation

The 3D unit cell was numerically analyzed by use of the finite element program ABAQUS (2004). The material in the cell was assumed to be elasto-plastic with isotropic hardening, with the uniaxial behavior defined in Section 3 below. ABAQUS (2004) makes use of an updated Lagrangian formulation to account for large deformations and employs a finite strain $J_2$ flow theory based on a co-rotational stress rate to account for rotations of the principal axes of deformation.

Symmetry allows for modeling of the $X_3 \geqslant 0$ half of the unit cell. A typical mesh with $\chi_0 = 0.2$ is shown in Fig. 5. It constists of 5184 20-node tri-quadratic elements with reduced integration of which 432 are located on the half spherical void surface. Periodic boundary conditions are applied on periodic points on the surfaces $X_2 = \pm D_0/2$. Four displacement measures $\delta_i$ $(i = 1,2,3,4)$ are introduced to describe the periodic and the homogeneous boundary conditions, respectively. The displacement boundary conditions can then be formulated as

$$\begin{aligned} \text{On } X_1 = \pm D_0: \quad & u_1(D_0, X_2, X_3) = -u_1(-D_0, X_2, X_3) = \delta_1, \\ & u_2(D_0, X_2, X_3) = -u_2(-D_0, X_2, X_3) + 2\delta_4, \\ & u_3(D_0, X_2, X_3) = u_3(-D_0, X_2, X_3), \end{aligned} \tag{14}$$

$$\begin{aligned} \text{On } X_2 = \pm D_0/2: \quad & u_1\left(X_1, \tfrac{D_0}{2}, X_3\right) = u_1\left(X_1, \tfrac{-D_0}{2}, X_3\right), \\ & u_2\left(X_1, \tfrac{D_0}{2}, X_3\right) = u_2\left(X_1, \tfrac{-D_0}{2}, X_3\right) + \delta_2, \\ & u_3\left(X_1, \tfrac{D_0}{2}, X_3\right) = u_3\left(X_1, \tfrac{-D_0}{2}, X_3\right), \end{aligned} \tag{15}$$

$$\begin{aligned} \text{On } X_3 = 0: \quad & u_3(X_1, X_2, 0) = 0, \\ \text{On } X_3 = D_0/2: \quad & u_3\left(X_1, X_2, \tfrac{D_0}{2}\right) = \delta_3/2. \end{aligned} \tag{16}$$

Here, the rates of $\delta_i$ are determined from the condition of loading under fixed stress ratios (4). To implement the special type of boundary condition we use the method suggested by Gudmundson and Faleskog (in preparation), where a full account of the method is given. The method will only briefly be outlined here.

Utilizing (14)–(16) in (9), the volume average of the deformation gradient and the velocity gradient, respectively, can be expressed as

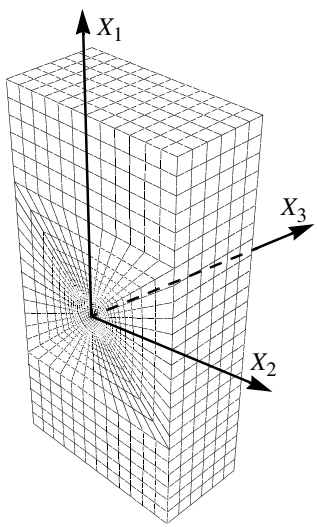


Fig. 5. Finite element mesh of one-half of the unit cell.

$$\bar{\mathbf{F}} = \begin{bmatrix} \frac{D_1}{D_0} & 0 & 0 \\ \frac{\delta_4}{D_0} & \frac{D_2}{D_0} & 0 \\ 0 & 0 & \frac{D_3}{D_0} \end{bmatrix}, \quad \bar{\mathbf{L}} = \dot{\bar{\mathbf{F}}}\bar{\mathbf{F}}^{-1} = \begin{bmatrix} \frac{\dot{\delta}_1}{D_1} & 0 & 0 \\ \frac{\dot{\delta}_4}{D_1} - \frac{\dot{\delta}_2}{D_2}\frac{\delta_4}{D_1} & \frac{\dot{\delta}_2}{D_2} & 0 \\ 0 & 0 & \frac{\dot{\delta}_3}{D_3} \end{bmatrix}, \tag{17}$$

where $D_1 = D_0 + \delta_1$, $D_2 = D_0 + \delta_2$ and $D_3 = D_0 + \delta_3$. The symmetric part of $\bar{\mathbf{L}}$ defines the volume average of the rate of deformation tensor $\mathbf{D}$ (13). Hill (1967, 1972) showed for the boundary conditions applicable here that the total work rate of the cell can be determined from the volume average values of the strain rate and stress, respectively, as

$$\dot{W} = V\Sigma_{ij}D_{ij} = \widehat{\mathbf{D}}^{\mathrm{T}}\widehat{\mathbf{\Sigma}}, \tag{18}$$

where $V = 2D_1D_2D_3$ and the column vectors

$$\widehat{\mathbf{\Sigma}} = \begin{bmatrix} V\Sigma_{11} \\ V\Sigma_{22} \\ V\Sigma_{33} \\ V\Sigma_{12} \end{bmatrix}, \quad \widehat{\mathbf{D}} = \begin{bmatrix} D_{11} \\ D_{22} \\ D_{33} \\ 2D_{12} \end{bmatrix} = \mathbf{Q}\dot{\boldsymbol{\delta}} \tag{19}$$

have been introduced. Here, $\mathbf{Q}$ is derived from $(17)_2$ and depends on $\delta_i$ and the initial dimensions of the cell. To enforce the linear constraints between the stress components, as defined by the ratios in (4), a set of generalized forces are introduced as

$$\mathbf{P} = \mathbf{C}^{\mathrm{T}}\widehat{\mathbf{\Sigma}} \text{ with } \mathbf{C} = [\mathbf{a}\ \mathbf{b}\ \mathbf{c}\ \mathbf{d}], \tag{20}$$

where $\mathbf{C}$ is a transformation matrix composed of the four orthonormal column vectors $\mathbf{a}$, $\mathbf{b}$, $\mathbf{c}$ and $\mathbf{d}$. In particular

$$\mathbf{a}^{\mathrm{T}} = \begin{bmatrix} \frac{1}{\psi_0} & \frac{\psi_2}{\psi_0} & \frac{\psi_3}{\psi_0} & \frac{\psi_4}{\psi_0} \end{bmatrix}, \quad \text{where } \psi_0 = \sqrt{1 + \psi_2^2 + \psi_3^2 + \psi_4^2}. \tag{21}$$

To proceed, we choose $\psi_2 = \psi_3 = \rho_n$ and $\psi_4 = \rho_s$ and note that the stress vector can be expressed as $\widehat{\mathbf{\Sigma}} = \mathbf{CP}$. The stress constraint (4) can now be satisfied by requiring that the generalized forces $P_2 = P_3 = P_4 = 0$. The stress vector then simplifies to $\widehat{\mathbf{\Sigma}} = \mathbf{a}P_1$. Hence, $P_1$ corresponds to the resulting generalized force aligned in the direction of $\widehat{\mathbf{\Sigma}}$, i.e., $\mathbf{a}$. The column vectors $\mathbf{b}$, $\mathbf{c}$ and $\mathbf{d}$ are given in the Appendix A.

Conjugate generalized displacement rates to $\mathbf{P}$ are defined as

$$\widehat{\mathbf{D}} = \mathbf{C}\dot{\mathbf{p}}, \quad \dot{\mathbf{p}}^{\mathrm{T}} = [\dot{p}_1\ \dot{p}_2\ \dot{p}_3\ \dot{p}_4]. \tag{22}$$

The conjugate properties of $\mathbf{P}$ and $\mathbf{p}$ are readily seen by inserting (20) and (22) into the work rate equation (18) giving $\dot{W} = \dot{\mathbf{p}}^{\mathrm{T}}\mathbf{P}$. It is thus convenient to introduce four new degrees of freedom $p_1$, $p_2$, $p_3$ and $p_4$ into the finite element model. These are coupled to the physical degrees of freedom in the unit cell model by inserting (22) into Eq. (19.2), which gives

$$\dot{\boldsymbol{\delta}} = \mathbf{Q}^{-1}\mathbf{C}\dot{\mathbf{p}}, \quad \mathbf{Q}^{-1} = \begin{bmatrix} D_0 + \delta_1 & 0 & 0 & 0 \\ 0 & D_0 + \delta_2 & 0 & 0 \\ 0 & 0 & D_0 + \delta_3 & 0 \\ 0 & \delta_4 & 0 & D_0 + \delta_1 \end{bmatrix}. \tag{23}$$

It should be noted that insertion of (23) into (14)–(16) constitutes a set of non-linear multi point constraint equations for the deformation of the 3D unit cell. Loading at fixed stress ratios can thus be achieved by applying the following boundary conditions

$$\dot{p}_1 = \dot{p}_0, \quad P_2 = P_3 = P_4 = 0, \tag{24}$$

where $\dot{p}_0$ is a prescribed value. Finally, this procedure was implemented into ABAQUS (2004) by utilizing the features provided in the user subroutines *EQUATION and *MPC.

Table 1
Material parameters for the mechanical properties

| Material | $\sigma_0$ (MPa) | $N$ | $\varepsilon_0$ | $\varepsilon_s$ | $\varepsilon_N$ |
|---|---|---|---|---|---|
| Weldox 420 | 418 | 0.018 | 0.0020 | 0.0084 | 0.0162 |
| Weldox 960 | 956 | 0.059 | 0.0046 | 0 | 0.0046 |

## 3. Material

The two materials considered are Weldox 420 and Weldox 960. The true stress–strain behavior, obtained from uniaxial tests, is given in Eq. (25) for both the materials, where $\sigma_0$ represents the initial yield stress, $N$ strain hardening exponent, $\varepsilon_s$ an offset strain, $\varepsilon_N$ a normalizing strain and $\varepsilon_0 = \sigma_0/E$. These material parameters are listed in Table 1.

$$\sigma = \begin{cases} E\varepsilon & \varepsilon \leqslant \varepsilon_0, \\ \sigma_0 & \varepsilon_0 \leqslant \varepsilon \leqslant \varepsilon_s + \varepsilon_N, \\ \sigma_0 \left(\frac{\varepsilon - \varepsilon_s}{\varepsilon_N}\right)^N & \varepsilon > \varepsilon_s + \varepsilon_N. \end{cases} \tag{25}$$

It is assumed that voids will nucleate from inclusions embedded in the matrix material. In Barsoum and Faleskog (2007), the average area fraction $A_f$ of inclusions is estimated by examination of 10 micrographs of polished surfaces for each material. It was found that $A_f = 0.0088$ for Weldox 420 and $A_f = 0.0060$ for Weldox 960. It should be noted that not all the inclusions will contribute to the nucleation of voids. Thus, it is assumed that the initial void volume fraction in the cell can be associated with a fraction $\eta$ of the inclusions. By equating $\eta A_f$ with the initial void volume fraction in the cell, an estimation of the initial ratio of void size to void spacing, $\chi_0$, can be obtained as

$$\chi_0 = \sqrt[3]{\frac{12}{\pi}\eta A_f}. \tag{26}$$

This gives $\chi_0 = 0.32 \times \sqrt[3]{\eta}$ for Weldox 420 and $\chi_0 = 0.28 \times \sqrt[3]{\eta}$ for Weldox 960. From Section 5 below it will be seen that an appropriate range for $\eta$ appears to be 0.004–0.03 for Weldox 420 and 0.04–0.15 for Weldox 960, respectively. Further details of the materials can be found in Barsoum and Faleskog (2007).

## 4. Model behavior and failure mechanisms

In this section, the general behavior of the model is explored and also how the two rupture mechanisms, internal necking and internal shearing, depends on $T$ and $\mu$. The strong influence that the stress triaxiality $T$ alone exerts on void growth and coalescence has been demonstrated in the past in cell studies under axisymmetric conditions (Andersson, 1977; Tvergaard, 1982b; Koplik and Needleman, 1988; Kuna and Sun, 1996; Søvik and Thaulow, 1997; Pardoen and Hutchinson, 2000), under plane strain conditions for cylindrical voids (Needleman, 1972; Tvergaard, 1981, 1982a; Faleskog and Shih, 1997) and for spherical voids (Faleskog et al., 1998; Gao et al., 2005). Other cell studies incorporate the possibility of shear deformation by employing fully periodic boundary conditions (Tvergaard, 1981, 1982a; Pijnenburg and Van der Giessen, 2001). The effects of the Lode parameter has also been studied on cells, but without allowing for shear deformation in the boundary conditions (Zhang et al., 2001; Gao and Kim, 2006).

### 4.1. Influence of $\mu$ on void growth and coalescence

The influence of the Lode parameter $\mu$ on void growth and coalescence will be elucidated first. This will be exemplified by results pertaining to an elastic, ideal plastic, medium strength material ($N = 0$ and $\varepsilon_0 = 0.002$ in (25)) and a fairly large $\chi_0 = 0.3$ to bring out the characteristic features related to variations in $\mu$. A constant

value of stress triaxiality $T = 1.0$ is chosen and five different $\mu$ values are considered, $\mu = 0$, $-0.33$, $-0.45$, $-0.65$, $-1$, ranging from generalized shear to generalized tension.

The macroscopic stress–strain response is strongly affected by $\mu$, as can be seen in Fig. 6(a). The onset of macroscopic yielding is significantly lower for generalized shear ($\Sigma_e = 0.90\sigma_0$ for $\mu = 0$) than for generalized tension ($\Sigma_e = 0.97\sigma_0$ for $\mu = -1$). For $\mu = 0$, the onset of yielding is primarily due to ligament shearing, which is controlled by the area fraction of voids given by $\pi\chi_0^2/4$. For $\mu = -1$ on the other hand, the onset of yielding is controlled by the volume fraction of voids (cf. Gurson, 1977), here estimated by $\pi\chi_0^3/12$. The latter also seems to govern the behavior for all cases where $\mu \leqslant -0.45$. For the remaining case $\mu = -0.33$, onset of yielding occurs between the two limiting cases of generalized tension and shear, respectively.

Significant softening, i.e., a noticeable decrease in stress $\Sigma_e$, is here associated with the onset of localization. Fig. 6(b) shows the ratio $\|\dot{\bar{\mathbf{F}}}\|/\|\dot{\mathbf{F}}^0\|$ vs. strain $E_e$, where it can be observed that the strain at localization (11) is decreasing with increasing values of $\mu$. For $\mu = -1$ localization occurs at about $E_e = 0.25$ and for $\mu \geqslant -0.33$ localization appears to coincide with the onset of yielding. Moreover, the softening rate increases with decreasing values of $\mu$ as can be seen Fig. 6(a). This is closely connected to the void growth rate, which can be appreciated from Fig. 6(c), showing the void volume ratio $V_v/V_{v0}$ (quotient between current to initial void volume) vs. strain $E_e$. The void growth rate corresponds to the slope of the curves in Fig. 6(c). For the case of generalized shear ($\mu = 0$) the void growth rate is initially high, but seems to vanish at about $E_e = 0.06$. For the case of

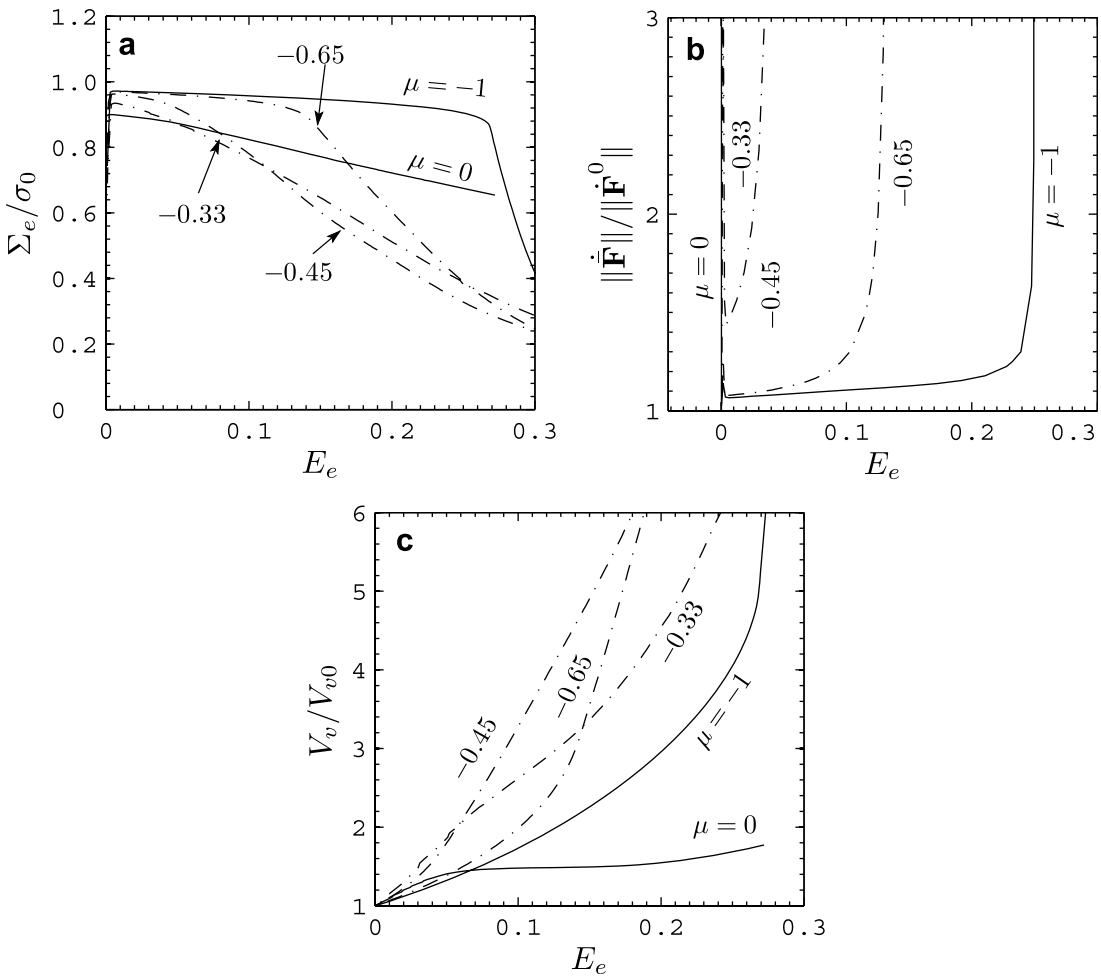


Fig. 6. Influence of the Lode parameter $\mu$ on the model behavior for an elastic–ideal plastic material ($N = 0$) with $\chi_0 = 0.3$ and a constant stress triaxiality $T = 1.0$. Showing (a) macroscopic effective stress, (b) the ratio $\|\dot{\bar{\mathbf{F}}}\|/\|\dot{\mathbf{F}}^0\|$ and (c) void growth vs. macroscopic effective strain.

generalized tension ($\mu = -1$) the void growth rate is initially lower than all other cases, but increases drastically at localization and there reaches a rate higher than all other cases. However, for strain values less than $E_e = 0.3$ the intermediate $\mu$-values $-0.45$ and $-0.65$ give rise to the largest void growth, $V_v/V_{v0}$ (the full range of $V_v/V_{v0}$ is not included in the graph).

At this juncture, readers should be reminded that the different behavior seen in Figs. 6(a)–(c) is solely due to the variations in the Lode parameter, since triaxiality is the same in all the examined cases. Thus, the value of $\mu$ has a profound effect on void growth and localization. In the present model, localization will act as a precursor to void coalescence, where two competing/co-operating modes can be identified from Fig. 6. For $\mu = -1$, void growth becomes extremely rapid at localization and coalescence is foreseen to take place by internal necking of intervoid ligaments. For $\mu = 0$, on the other hand, coalescence is inclined to take place by shearing off intervoid ligaments due to the limited void growth. Next, the two different mechanisms will be described where the material behavior and the cell parameters are chosen to resemble the two materials used in the experiments.

### 4.2. Void coalescence by internal necking

To simulate the rupture mechanism associated with coalescence by internal necking of intervoid ligaments, data is taken from the material Weldox 960, with $\chi_0 = 0.2$. The load case considered corresponds to a triaxiality of $T = 1.0$ and a Lode parameter near generalized tension, $\mu = -0.85$.

Figs. 7(a and b) show the stress $\Sigma_e$ and the ratio $\|\dot{\bar{\mathbf{F}}}\|/\|\dot{\mathbf{F}}^0\|$ plotted vs. the strain $E_e$. The deformation is virtually homogeneous for strains less than 0.09, since $\|\dot{\bar{\mathbf{F}}}\|/\|\dot{\mathbf{F}}^0\| \approx 1$. For increasing levels of strain, the deformation gradually shifts to the layer of voids, and localization occurs at $E_e = 0.39$. This causes a drastic drop in the effective stress as seen in Fig. 7(a), where the localization point is marked with a solid circle. The localization event is here accompanied by a drastic increase in void volume as is notable in Fig. 7(c), showing the ratio $V_v/V_{v0}$ vs. $E_e$.

Fig. 7(d) show the deformation measures $\bar{q}_1$ and $\bar{q}_2$ vs. $E_e$. These measures defined in Eq. (10) corresponds to the non-uniform normal and shear deformation, respectively, associated with localization. A geometric interpretation is illustrated by the deformed mesh shown in Fig. 7(e). The rate of $\bar{q}_1$ increases drastically after the onset of localization as expected. $\bar{q}_2$ follows a similar history. Even though the mode of coalescence then appears to be a combination of the two modes discussed above, coalescence occurs by internal necking of intervoid ligaments in this case. This is underlined by the deformed mesh of the unit cell shown in Fig. 7(e), where the undeformed mesh also is shown as a reference. The deformed mesh belongs to the load point marked by an open circle in the localization regime as depicted in Fig. 7(a). In addition, the deformed mesh representing this coalescence mode is envisioned to be consistent with the morphology observed in the fractograph shown in Fig. 2(a), where final rupture has occurred by the internal necking mechanism.

### 4.3. Void coalescence by internal shearing

In a stress state near generalized shear ($\mu \to 0$) and low triaxiality, growth of voids is limited. Here, the final rupture mechanism is mainly due to internal shearing between voids. To simulate this mechanism, data is again taken from the material Weldox 960 and $\chi_0 = 0.2$, but with the stress state parameters $T = 0.5$ and $\mu = -0.15$.

Along with the previous case, the deformation is virtually homogeneous for strains less than 0.09, as can be observed from Figs. 8(a and b) showing $\Sigma_e$ and $\|\dot{\bar{\mathbf{F}}}\|/\|\dot{\mathbf{F}}^0\|$ vs. $E_e$. At this strain level ($E_e = 0.09$), in contrast to the previous case, an early tendency to localization can be observed by the abrupt increase in the ratio $\|\dot{\bar{\mathbf{F}}}\|/\|\dot{\mathbf{F}}^0\|$. However, localization is put on hold by material strain hardening and does not occur until $E_e = 0.6$, as is seen in Fig. 8(b). The localization point is also marked by a solid circle in the stress–strain curve shown in Fig. 8(a). From Fig. 8(c) it is noted that void growth ($V_v/V_{v0}$) is essentially linear with respect to $E_e$ up to localization, where it seems to saturate at a value of about 2.2.

The non-uniform shear deformation $\bar{q}_2$ starts to increase at a constant rate at the subsidiary localization ($E_e = 0.09$), and becomes practically unbounded at localization ($E_e = 0.6$), as can be observed in Fig. 8(d). At the same time, the non-uniform normal deformation $\bar{q}_1$ is negligible. Here, coalescence occurs by extensive localized shear deformation in the ligaments between voids and essentially no void growth. The deformed

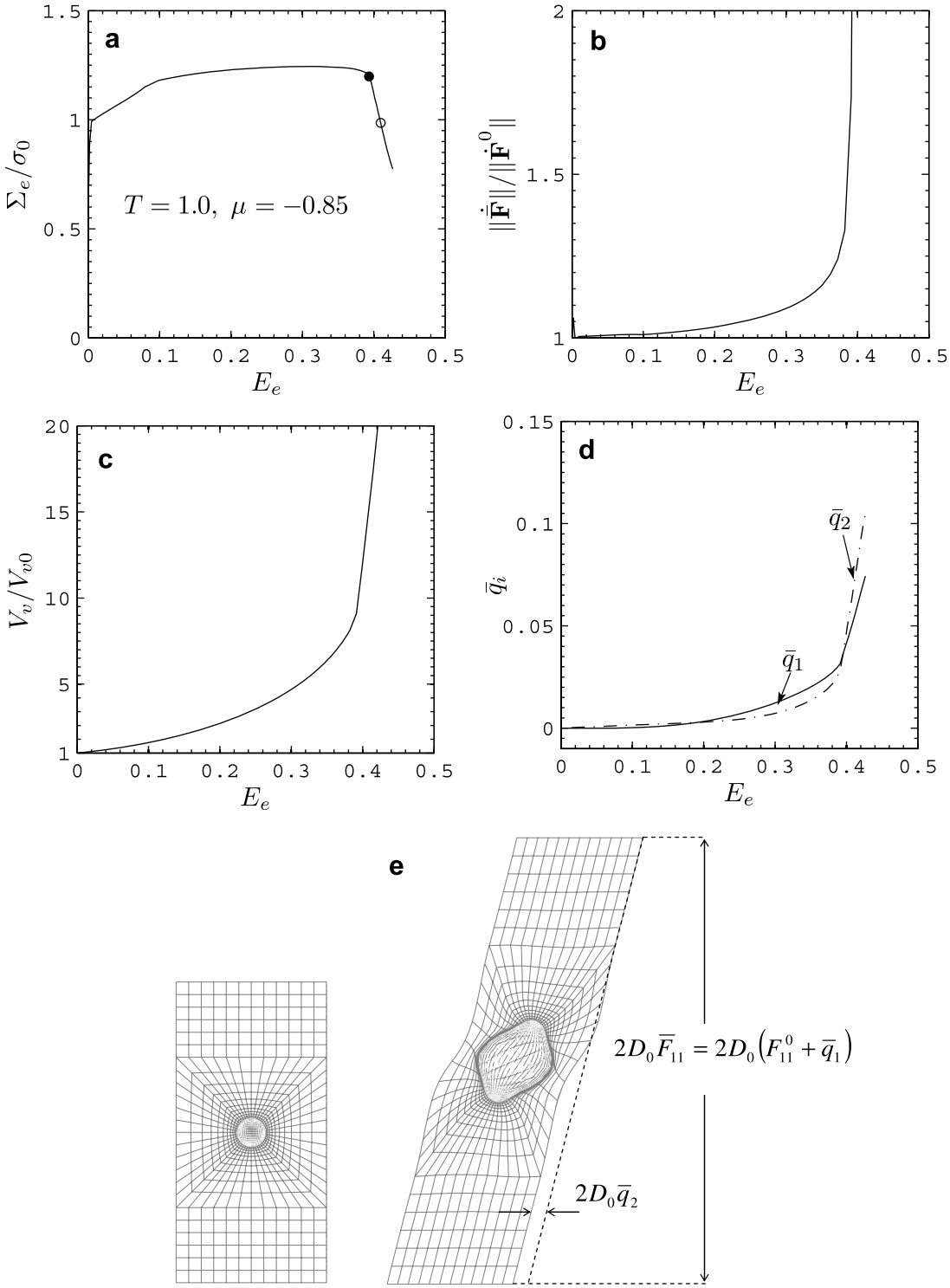


Fig. 7. Illustration of void coalescence by internal necking for the material Weldox 960 with $\chi_0 = 0.2$, $\mu = -0.85$ and $T = 1.0$. (a) Macroscopic effective stress, (b) the ratio $\|\dot{\bar{\mathbf{F}}}\|/\|\dot{\bar{\mathbf{F}}}^0\|$, (c) void growth and (d) $\bar{q}_1$ and $\bar{q}_2$ of Eq. (10) vs. macroscopic effective strain $E_e$. (e) The undeformed and deformed mesh showing this coalescence mode. The open circle in (a) represents the instance of the deformed mesh in (e) and the solid circle indicates the onset of localization.

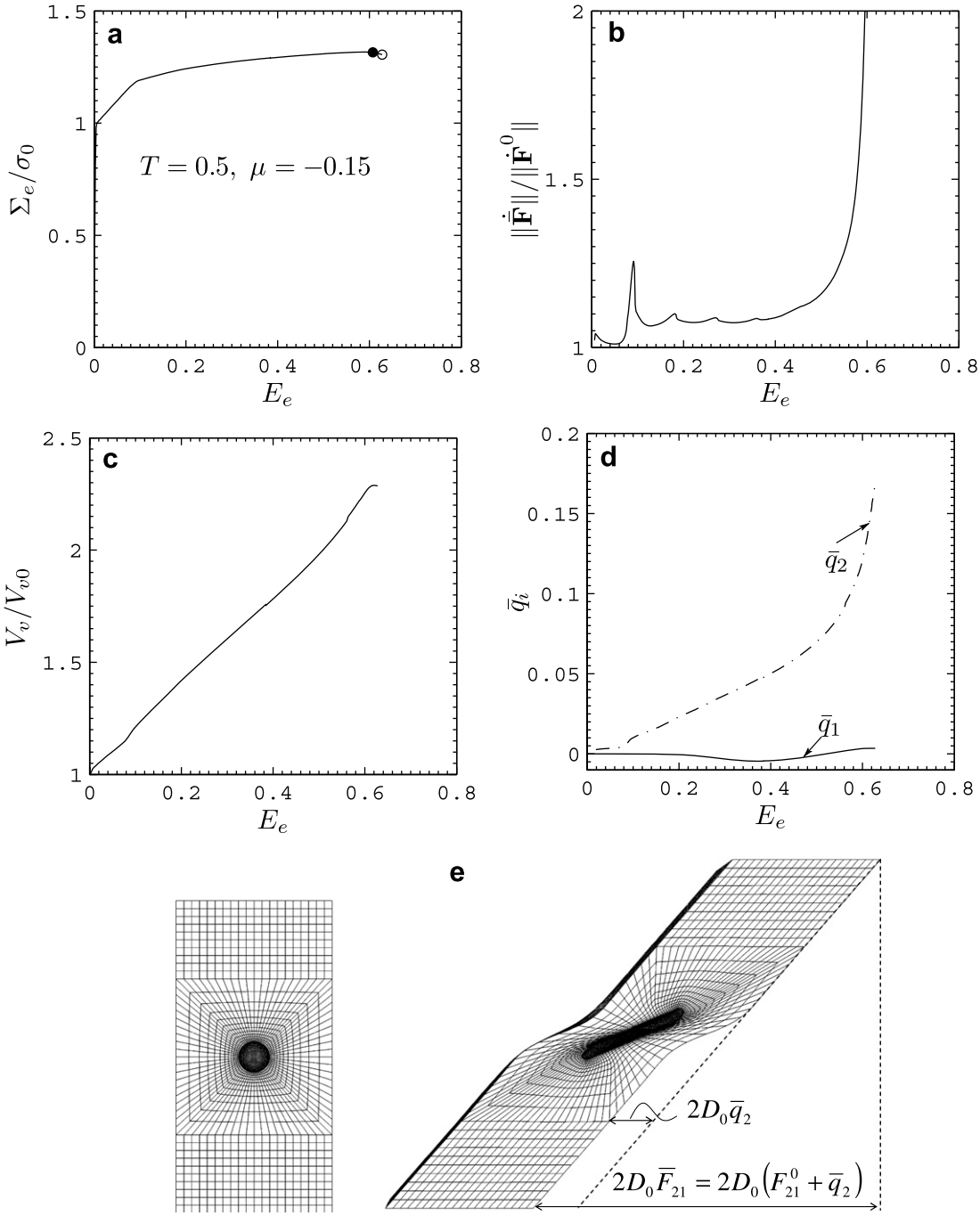


Fig. 8. Illustration of void coalescence by internal shearing for the material Weldox 960 with $\chi_0 = 0.2$, $\mu = -0.15$ and $T = 0.5$. (a) Macroscopic effective stress, (b) the ratio $\|\dot{\bar{\mathbf{F}}}\|/\|\dot{\mathbf{F}}^0\|$, (c) void growth and (d) $\bar{q}_1$ and $\bar{q}_2$ of Eq. (10) vs. macroscopic effective strain $E_e$. (e) The undeformed and deformed mesh showing this coalescence mode. The open circle in (a) represents the instance of the deformed mesh in (e) and the solid circle indicates the onset of localization.

mesh in Fig. 8(e), taken at the load level shown by the open circle in Fig. 8(a), illustrates this mode of coalescence. This rupture mode is consistent with the shear dimple rupture mechanism observed in the fractograph in Fig. 2(b), showing small elongated shear dimples similar to the deformed shape in Fig. 8(e).

Finally, it is noted that before the onset of localization the major axes of the evolving void shapes in Figs. 7 and 8(e) are roughly aligned with the directions of the principal stresses in the respective case. The latter directions are fixed in the present analysis due to the constraint (4). At localization, the void in Fig. 7(e) seems to grow with its major axis in the bisector direction of the $x_1$–$x_2$ plane, since $\bar{q}_1 \approx \bar{q}_2$, whereas the void in Fig. 8(e) primarily rotates toward the $x_2$-axis, with constant void volume.

## 5. Micromechanics analysis of the experiments and discussion

The micromechanics model will, here, be applied to analyze the experiments carried out in Barsoum and Faleskog (2007) on the double notched tube specimen pictured in Fig. 1. The properties of the two materials tested are listed in Table 1. The loading condition of the unit cell, Eqs. (4) and (7), was chosen such that it resembles the stress state at failure in the centre of the notch shown in Fig. 1(b). The stress state, $T$ vs. $\mu$, at failure for the two materials is depicted in Fig. 9, which were obtained from the experimental work by Barsoum and Faleskog (2007). Three different initial void size to void spacing ratios were considered, $\chi_0 = 0.05$, 0.10 and 0.15, which corresponds to void volume fractions $f_0 = 0.33 \times 10^{-4}$, $0.26 \times 10^{-3}$ and $0.88 \times 10^{-3}$,

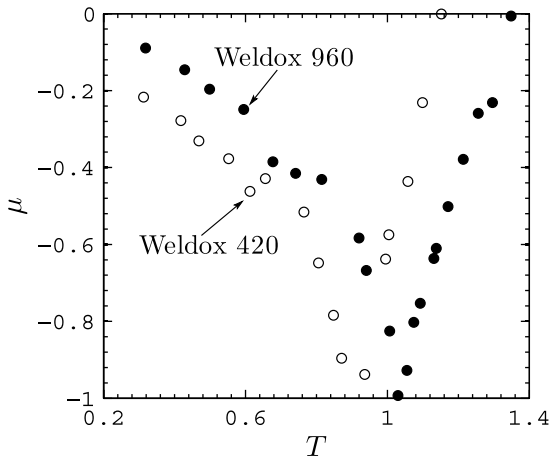


Fig. 9. The Lode parameter $\mu$ vs. stress triaxiality $T$ in the centre of the notch at failure (cf. Barsoum and Faleskog, 2007). Open circles pertain to Weldox 420 and solid circles pertain to Weldox 420 and solid circles pertain to Weldox 960.

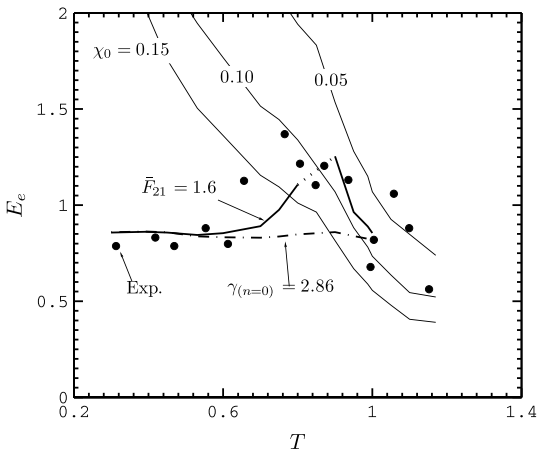


Fig. 10. Failure locus for Weldox 420, where the macroscopic effective strain $E_e$ at failure is plotted vs. stress triaxiality $T$. The solid circles represents experimental results. The three thin lines indicate failure by localization according to Eq. (11) and the thick line indicates failure when $\bar{F}_{21} = 1.6$ is attained and the dash-dotted line indicates to failure when $\gamma_{(n=0)} = 2.86$ in Eq. (28) is attained.

respectively. In relation to the content of inclusions in the two materials, this means that only a fraction of about 15% or less of the inclusions will participate in the nucleation of voids at such low loads that they can be regarded as present from the beginning, see Section 3.

The outcomes of the micromechanics analyses are summarized and compared with the experimental results in Fig. 10 for Weldox 420 and in Fig. 11 for Weldox 960, where critical values of strain $E_e$ are plotted vs. triaxiality $T$. The solid circles are experimental data and represent the effective plastic strain in the centre of the notch of a specimen at failure. In Figs. 10 and 11, $E_e$ represents the total effective strain, however, this is only of order $\varepsilon_0$ larger than the effective plastic strain and the difference is therefore negligible. The thin solid lines, corresponding to the three different $\chi_0$ values, are theoretical curves from the micromechanics model that indicate failure by localization according to Eq. (11), which marks the onset of void coalescence and subsequent failure by ductile rupture. Note that the theoretical curves captures the experimental results well for triaxiality values larger than about 0.8 for both materials. The experimental results exhibit some scatter, but the failure points pertaining to Weldox 420 appears to be well described by the theoretical curves with $0.05 < \chi_0 < 0.10$, and the failure points pertaining to Weldox 960 appears to be well described by the theoretical curves with $0.10 < \chi_0 < 0.15$. From Eq. (26) the fraction of inclusions participating in nucleating voids can then be estimated to be in the range 0.4–3% for Weldox 420 and in the range 4–15% for Weldox 960.

In the higher triaxiality range discussed above, the behavior of a unit cell in the post-localization regime is characterized by a dramatic decrease in stress $\Sigma_e$ and a significant increase in void volume $V_v/V_{v0}$. This can be ascertained by Fig. 12 showing the effective stress–strain behavior in (a) and void growth vs. effective strain in (b) for Weldox 420 with $\chi_0 = 0.1$. The four curves belong to the $T$ values: 0.53, 0.7, 0.9 and 1.1, where the two lower $T$ values will be dealt with later. The open circles indicate the onset of localization. Note that also the $T = 1.1$ case exhibits a dramatic drop in $\Sigma_e$ and a significant increase in $V_v/V_{v0}$, even though $\mu$ is approaching zero. Not shown here, but post-localization in this triaxiality range is also accompanied by a noticeable increase in $\bar{q}_1$. Increase in $\bar{q}_1$ and $V_v/V_{v0}$ is indicative of the rupture mechanism described as void coalescence by internal necking, which also agrees with the type of rupture mechanism observed in the fractographical investigation reported in Barsoum and Faleskog (2007) for this range in triaxiality. Thus, it appears that final rupture occurs by void coalescence through internal necking in the materials investigated here when stress triaxiality is high enough regardless the value of $\mu$. Onset of void coalescence described by the localization criterion (11) can be viewed as a generalization of the change of deformation to an uniaxial straining mode that characterizes void coalescence under axisymmetric conditions as found by Koplik and Needleman (1988).

In the low triaxiality regime ($T < 0.8$), the solid lines representing the localization criterion do not at all capture the experimental outcome. Failure occurs at much lower strain levels than what would be predicted by Eq. (11). In fact, the strain at failure decreases somewhat with decreasing stress triaxiality and the layer of

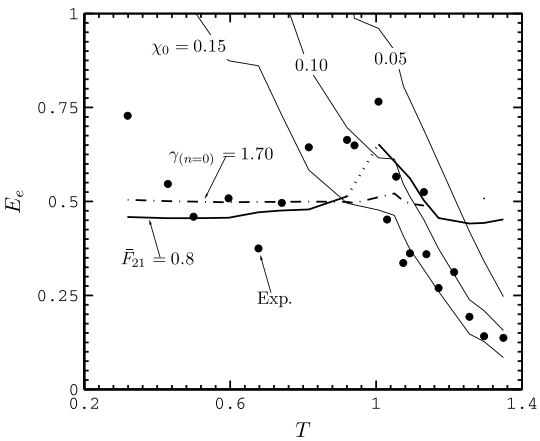


Fig. 11. Failure locus for Weldox 960, where the macroscopic effective strain $E_e$ at failure is plotted vs. stress triaxiality $T$. The solid circles represents experimental results. The three thin lines indicate failure by localization according to Eq. (11), the thick line indicates failure when $\bar{F}_{21} = 0.8$ is attained and the dash-dotted line indicates to failure when $\gamma_{(n=0)} = 1.70$ in Eq. (28) is attained.

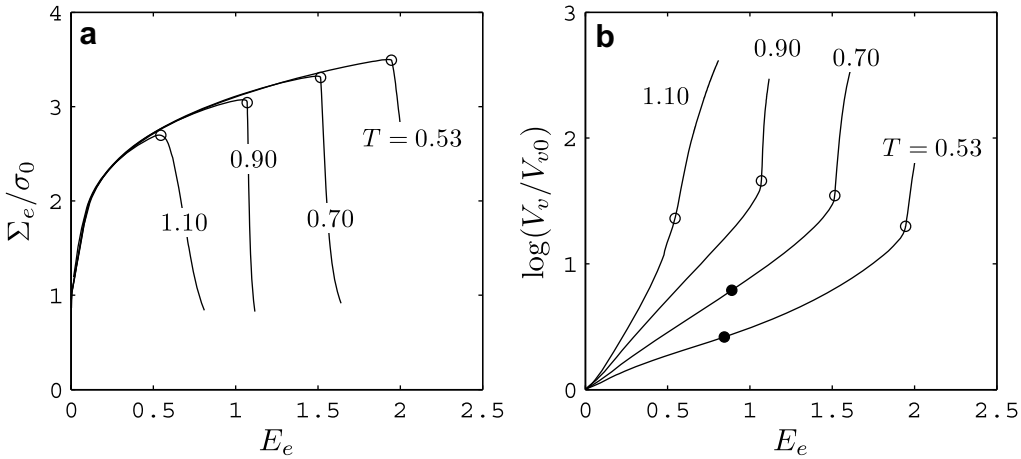


Fig. 12. Behavior of the unit cell in the post-localization regime for Weldox 420 with $\chi_0 = 0.1$. (a) Macroscopic effective stress and (b) void growth vs. macroscopic effective strain $E_e$. The open circles indicates the onset of localization and solid circles indicates when $\bar{F}_{21} = 1.6$ is attained.

pre-existing voids does not seem to play a role in the onset of fracture. This abrupt change in behavior is accompanied by an abrupt change in the Lode parameter as seen from Fig. 9. Here, a transition in the rupture mechanisms was observed in the experiments and the deformation across the notch of the specimen (see Fig. 1) became dominated by shearing as the triaxiality decreased. Building on this observation, a simple criterion based on the attainment of a critical shear deformation was explored here. Within the context of the micromechanics model employed, such a criterion was realized by assuming that failure occurs when the shear component $\bar{F}_{21}$ of the volume average of the deformation gradient, Eq. (10) or (17), reaches a critical value. The critical value was chosen such that the strain at failure captures the experimental results when $T < 0.6$ for Weldox 420 and when $T < 0.8$ for Weldox 960, and was found to be 1.6 for Weldox 420 and 0.8 for Weldox 960. The difference between the localization and the critical shear deformation criterion, respectively, can be seen for material Weldox 420 in Fig. 12(b), where the filled circles mark the attainment of $\bar{F}_{21} = 1.6$ prior to the onset of localization (open circles) for the cases $T = 0.53$ and 0.70. The thick solid lines in Figs. 10 and 11 represent the critical shear deformation criterion, and it can be observed that the accordance with the experimental results of Weldox 420 is very good, whereas the accordance with the experimental results of Weldox 960 is less apparent. One may also note that the thick solid line at some instances is replaced by a dashed line. This indicates that no solution was found in the strain range considered in Figs. 10 and 11, which is due to the near axisymmetric conditions prevailing here, with the consequence that $\bar{F}_{21}$ does not attain large values. In this low triaxiality regime, the measures of localized deformation $\bar{q}_1$ and $\bar{q}_2$ are as good as zero at the instance where the shear deformation criterion predicts failure, i.e., $\bar{F}_{21}$ is virtually equal to the corresponding component of the uniform deformation gradient, i.e., $F^0_{21}$. The physical relevance and a generalization of the simplistic criterion based on shear deformation will be discussed next.

Despite the fact that the pre-existing voids do not seem to trigger failure at this lower triaxiality range, the inspection of the fractured specimens made in Barsoum and Faleskog (2007) reveal that the fracture surfaces to a large extent are covered with small elongated shear dimples as shown in Fig. 2(b). The probable cause for this is that failure is triggered by an extensive nucleation of voids occurring at a rather narrow interval in strain $E_e$. This kind of strain driven nucleation behavior is observed in experiments and discussed by Goods and Brown (1979) and Fisher and Gurland (1981). Further discussion on void nucleation can be found in the review articles by Van Stone et al. (1985) and Garrison and Moody (1987). There is also evidence that a sudden burst of void nucleation can trigger shear localization in some high strength steels as recognized by Hutchinson and Tvergaard (1989). If a burst of void nucleation is responsible for the failure observed in the experiments, it appears to be rather insensitive to variations in the parameters $T$ and $\mu$, with the exception of $\mu$ approaching $-1$, which corresponds to axisymmetric conditions. A material is generally far more resistant to shear band formation under axisymmetric (generalized tension) conditions than under plane strain (generalized shear) conditions. Chu and Needleman (1980) have suggested a simple model for void nucleation within a

continuum framework that allows for nucleation under an arbitrary narrow interval in strain. Void nucleation was not accounted for in the present micromechanics model.

In an attempt to generalize the simple criterion used here based on the shear component of the volume average of the deformation gradient, $\bar{F}_{21}$, we make use of the a generalized strain tensor defined as

$$\mathbf{E}_{(n)} = \begin{cases} \ln \bar{\mathbf{U}} & n = 0, \\ \frac{1}{n}(\bar{\mathbf{U}}^n - \mathbf{I}) & n > 0, \end{cases} \tag{27}$$

where $\bar{\mathbf{U}}$ is the average of the right Cauchy–Green stretch tensor over some representative volume and $\mathbf{I}$ is the second order unit tensor. For the special cases $n = 0$, 1 and 2, the strain tensors Hencky, Biot and Green–Lagrange, respectively, are obtained. A generalized measure of the maximum shear deformation can then be defined as

$$\gamma_{(n)} = \begin{cases} \ln(\lambda_1/\lambda_3) & n = 0, \\ \frac{1}{n}(\lambda_1^n - \lambda_3^n) & n > 0, \end{cases} \tag{28}$$

where $\lambda_1 > \lambda_2 > \lambda_3$ are the eigenvalues/principal stretches of $\bar{\mathbf{U}}$. Here, failure was assumed to occur when $\gamma_{(n=0)}$ reached a critical value chosen such that the strain at failure captures the experimental results in the low stress triaxiality regime. The critical value of $\gamma_{(n=0)}$ was found to be 2.86 for Weldox 420 and 1.70 for Weldox 960. This failure criterion is signified by the thick dash-dotted line in Figs. 10 and 11. The agreement with the experimental results is acceptable. However, this generalized shear deformation criterion does not capture the up going trend in failure strain near the transition region. The other two measures $\gamma_{(n=1)}$ and $\gamma_{(n=2)}$ were also checked here, but did not improve the predictions as compared to $\gamma_{(n=0)}$.

## 6. Conclusions

In the present study, micromechanics modelling of rupture mechanisms in combined tension and shear is performed. The micromechanics model consists of a unit cell containing a single void allowing for fully periodic boundary conditions, which enables examination of two modes of void coalescence leading to ductile fracture. The unit cell is loaded under proportional stressing conditions allowing for arbitrary ratios of macroscopic stresses in terms of stress triaxiality and the Lode parameter. The present study is concluded by the following points:

- The influence of the Lode parameter on void growth and coalescence can be significant.
- Two distinctly different rupture mechanisms are predicted with the micromechanics model.
- The void coalescence by internal necking is predicted by a localization criterion, which can be view as a generalization of the change of deformation to a uniaxial straining mode that characterizes void coalescence under axisymmetric conditions (cf. Koplik and Needleman, 1988).
- Shear failure is predicted by a critical shear deformation criterion, where pre-existing voids do not play a significant role.
- The micromechanics model, extended with the shear deformation criterion, captures the experimental trends well.

## Acknowledgment

The authors acknowledge the financial support from the Swedish Research Council under contract 621-2004-5121.

## Appendix A

The elements of the orthogonal column vectors in matrix $\mathbf{C}$ are given here. Orthogonality gives 9 conditions for the 12 elements in the vectors $\mathbf{b}$, $\mathbf{c}$ and $\mathbf{d}$. Thus, there is no unique way of constructing these vectors, and

therefore three parameters, $\beta_1$, $\beta_2$ and $\beta_3$, are introduced. In order to make the elements of **C** real, these parameters must be chosen in the interval: $0 < \beta_i < 1$. Starting with the elements of **d**, the conditions $\mathbf{a}^T\mathbf{d} = 0$, $\mathbf{d}^T\mathbf{d} = 1$ and requirement of **d** being real, gives

$$d_4 = \pm\frac{1}{\psi_0}\sqrt{\beta_1\beta_2(\psi_0^2 - \psi_4^2)}, \quad d_3 = \pm\sqrt{\frac{\beta_1}{\psi_0^2 - \psi_4^2}}\left[\sqrt{(1+\psi_2^2)(1-\beta_2)} - \frac{\psi_3\psi_4}{\psi_0}\sqrt{\beta_2}\right],$$

$$d_2 = -\frac{\psi_2(\psi_3 d_3 + \psi_4 d_4)}{1+\psi_2^2} \pm \sqrt{\frac{1-\beta_1}{1+\psi_2^2}}, \quad d_1 = -(\psi_2 d_2 + \psi_3 d_3 + \psi_4 d_4).$$

Continuing with the elements of **c**, the conditions $\mathbf{a}^T\mathbf{c} = \mathbf{d}^T\mathbf{c} = 0$, $\mathbf{c}^T\mathbf{c} = 1$ and requirement of **c** being real, gives

$$c_4 = \pm\sqrt{\frac{\beta_3 g_0^2 G_1}{G_1 G_3 - G_2^2}}, \quad c_3 = \pm\sqrt{\frac{g_0^2}{G_1}}\left[\sqrt{1-\beta_3} - G_2\sqrt{\frac{\beta_3}{G_1 G_3 - G_2^2}}\right], \quad c_2 = -(c_3 g_3 + c_4 g_4)/g_0,$$

$$c_1 = (c_3 g_1 + c_4 g_2)/g_0,$$

where

$$G_1 = g_0^2 + g_1^2 + g_3^2, \quad G_2 = g_1 g_2 + g_3 g_4, \quad G_3 = g_0^2 + g_2^2 + g_4^2; \quad g_0 = \psi_2 d_1 - d_2$$

$$= \mp\sqrt{(1-\beta_1)(1+\psi_2^2)}, \quad g_1 = \psi_3 d_2 - \psi_2 d_3, \quad g_2 = \psi_4 d_2 - \psi_2 d_4, \quad g_3 = \psi_3 d_1 - d_3,$$

$$g_3 = \psi_4 d_1 - d_4.$$

Finally, the elements of **b** are determined from the conditions $\mathbf{a}^T\mathbf{b} = \mathbf{c}^T\mathbf{b} = \mathbf{d}^T\mathbf{b} = 0$ and $\mathbf{b}^T\mathbf{b} = 1$ as

$$b_4 = \pm\frac{1}{\sqrt{1+\mathbf{h}^T\mathbf{h}}}, \quad \begin{bmatrix} b_1 \\ b_2 \\ b_3 \end{bmatrix} = -b_4\mathbf{h},$$

where

$$\mathbf{h} = \mathbf{H}^{-1}\begin{bmatrix} \psi_4 \\ c_4 \\ d_4 \end{bmatrix}, \quad \mathbf{H} = \begin{bmatrix} 1 & \psi_2 & \psi_3 \\ c_1 & c_2 & c_3 \\ d_1 & d_2 & d_3 \end{bmatrix}.$$

The positive roots and $\beta_1 = \beta_2 = \beta_3 = 0.5$ were employed in the present study.

## References


ABAQUS, 2004. Standard-User's Manual, Version 6.4. Hibbit, Karlsson and Sorensen, Inc., Providence, RI.

Andersson, H., 1977. Analysis of a model for void growth and coalescence ahead of a moving crack tip. Journal of Mechanics and Physics of Solids 25, 217–233.

Bao, Y., Wierzbicki, T., 2004. On the fracture locus in the equivalent strain and stress triaxiality space. International Journal of Mechanical Sciences 46, 81–98.

Barsoum, I., Faleskog, J., 2007. Rupture mechanisms in combined tension and shear—Experiments. International Journal of Solids and Structures 44, 1768–1786.

Chu, C.C., Needleman, A., 1980. Void nucleation effects in biaxially stretched sheets. Journal of Engineering Materials and Technology 102, 249–256.

Faleskog, J., Gao, X., Shih, C.F., 1998. Cell model for nonlinear fracture analysis— I. Micromechanics calibration. International Journal of Fracture 89, 355–373.

Faleskog, J., Shih, C.F., 1997. Micromechanics of coalescence—I. Synergistic effects of elasticity, plastic yielding and multi-size-scale voids. Journal of Mechanics and Physics of Solids 45, 21–50.

Fisher, J.R., Gurland, J., 1981. Void nucleation in spherodized carbon steels part 1: experiments. Metal Science 15, 185–192.

Gao, X., Kim, J., 2006. Modeling of ductile fracture: significance of void coalescence. International Journal of Solids and Structures 43, 6277–6293.

Gao, X., Wang, T., Kim, J., 2005. On ductile fracture initiation toughness: effects of void volume fraction, void shape and void distribution. International Journal of Solids and Structures 42, 5097–5117.

Garrison Jr., W.M., Moody, N.R., 1987. Ductile fracture. Journal of Physics and Chemistry of Solids 48, 1035–1074.
Goods, S.H., Brown, L.M., 1979. The nucleation of cavities by plastic deformation. Acta Metallurgica 27, 1–15.
Gudmundson, P., Faleskog. J., in preparation. Control of average stress and strain measures in micromechanical finite elements calculations. Royal Institute of Technology, Department of Solid Mechanics.
Gurson, A.L., 1977. Continuum theory of ductile rupture by void nucleation and growth: Part I—Yield criteria and flow rules for porous ductile media. Journal of Engineering Materials and Technology, 2–17.
Hill, R., 1967. The essential structure of constitutive laws for metal composites and polycrystals. Journal of Mechanics and Physics of Solids 15, 79–95.
Hill, R., 1972. On constitutive macro-variables for heterogeneous solids at finite strain. Proceedings of the Royal Society of London A 326, 131–147.
Hutchinson, J.W., Tvergaard, V., 1989. Softening due to void nucleation in metals. In: Wei, R.P., Gangloff, R.P. (Eds.), Fracture Mechanics: Perspective and Directions (20th Symposium), ASTM STP 1020. American Society for Testing of Materials, Philadelphia, pp. 61–83.
Koplik, J., Needleman, A., 1988. Void growth and coalescence in porous plastic solids. International Journal of Solids and Structures 24, 835–853.
Kuna, M., Sun, D.Z., 1996. Three-dimensional cell model analyses of void growth. International Journal of Fracture 81, 235–258.
Marciniak, K., Kuczynski, K., 1967. Limit strains in the process of stretch forming sheet metal. International Journal of Mechanical Sciences 9, 609–620.
Needleman, A., 1972. Void growth in elastic–plastic medium. Journal of Applied Mechanics 39, 964–970.
Needleman, A., Rice, J.R., 1978. Limits to ductility set by plastic flow localization. In: Koistinen, D.P., Wang, N.-M. (Eds.), Mechanics of Sheet Metal Forming. Plenum Publishing, New York, pp. 237–267.
Needleman, A., Tvergaard, V., 1984. An analysis of ductile rupture in notched bars. Journal of the Mechanics and Physics of Solids 32, 461–490.
Needleman, A., Tvergaard, V., 1992. Analysis of plastic flow localization in metals. Applied Mechanics Reviews 45, S3–S18.
Pardoen, T., Hutchinson, J.W., 2000. An extended model for void growth and coalescence. Journal of Mechanics and Physics of Solids 48, 2467–2512.
Pijnenburg, K.G.W., Van der Giessen, E., 2001. Macroscopic yield in cavitated polymer blends. International Journal of Solids and Structures 38, 3575–3598.
Rice, J.R., 1977. The localization of plastic deformation. In: Koiter, W.T., (Ed.), Theoretical and Applied Mechanics, North-Holland, pp. 207–220.
Saje, M., Pan, J., Needleman, A., 1982. Void nucleation effects on shear localization in porous solids. International Journal of Fracture 19, 163–182.
Søvik, O.P., Thaulow, C., 1997. Growth of spheroidal voids in elastic–plastic solids. Fatigue and Fracture of Engineering Materials and Strutures 20, 1731–1744.
Tvergaard, V., Needleman, A., 1984. Analysis of the cup-cone fracture in a round tensile bar. Acta Metallurgica 32, 157–169.
Tvergaard, V., 1981. Influence of voids on shear band instabilities under plane strain conditions. International Journal of Fracture 17, 389–407.
Tvergaard, V., 1982a. Ductile fracture by cavity nucleation between larger voids. Journal of the Mechanics and Physics of Solids 30, 265–286.
Tvergaard, V., 1982b. On localization in ductile materials containing spherical voids. International Journal of Fracture 18, 237–252.
Van Stone, R.H., Cox, T.B., Low, J.R., Psioda, J.A., 1985. Microstructural aspects of fracture by dimpled rupture. International Metals Reviews 30, 157–179.
Wierzbicki, T., Bao, Y., Lee, Y.W., Bai, Y., 2005. Calibration and evaluation of seven fracture models. International Journal of Mechanical Sciences 47, 719–743.
Yamamoto, H., 1978. Conditions for shear localization in the ductile fracture of void-containing materials. International Journal of Fracture 14, 347–365.
Zhang, K.S., Bai, J.B., Francois, D., 2001. Numerical analysis of the influence of the lode parameter on void growth. International Journal of Solids and Structures 38, 5847–5856.